PHOTONICS Research

Coupling ideality of standing-wave supermode microresonators

Min Wang,[1,2,†] Yuechen Lei,[1,2,†] Zhi-Gang Hu,[1,2] Chenghao Lao,[1,3] Yuanlei Wang,[1,3] Xin Zhou,[1,2] Jincheng Li,[1,4] Qi-Fan Yang,[3,5,7] ⓘ AND Bei-Bei Li[1,2,6,*] ⓘ

[1]*Beijing National Laboratory for Condensed Matter Physics, Institute of Physics, Chinese Academy of Sciences, Beijing 100190, China*
[2]*University of Chinese Academy of Sciences, Beijing 100049, China*
[3]*State Key Laboratory for Mesoscopic Physics and Frontiers Science Center for Nano-optoelectronics, School of Physics, Peking University, Beijing 100871, China*
[4]*School of Physics, Beihang University, Beijing 100191, China*
[5]*Collaborative Innovation Center of Extreme Optics, Shanxi University, Taiyuan 030006, China*
[6]*Songshan Lake Materials Laboratory, Dongguan 523808, China*
[7]*e-mail: leonardoyoung@pku.edu.cn*
[†]*These authors contributed equally to this work.*
Corresponding author: libeibei@iphy.ac.cn

Standing-wave supermode microresonators that are created through the strong coupling between counter-propagating modes have emerged as versatile platforms for sensing and nonlinear optics. For example, these microresonators have shown potential in nanoparticle sizing and counting, as well as enhancing the single-photon optomechanical coupling rate of stimulated Brillouin scattering. However, it has been observed that the relation between the mode linewidth and on-resonance transmission of the split supermodes differs obviously from that of the non-split modes. This behavior is typically quantified by the coupling ideality (I), which remains inadequately explored for the standing-wave supermodes. In this study, we theoretically and experimentally investigate the coupling ideality of standing-wave supermodes in a commonly employed configuration involving a SiO_2 microresonator side-coupled to a tapered fiber. Our findings demonstrate that, even with a single-mode tapered fiber, the coupling ideality of the standing-wave supermodes is limited to 0.5, due to the strong backscattering-induced energy loss into the counter-propagating direction, resulting in an additional equivalent parasitic loss. While achieving a coupling ideality of 0.5 presents challenges for reaching over-coupled regimes, it offers a convenient approach for adjusting the total linewidth of the modes while maintaining critically-coupled conditions. © 2024 Chinese Laser Press

1. INTRODUCTION

Supermodes in whispering-gallery-mode (WGM) microresonators have been extensively explored owing to their ability to engineer light fields, which can be categorized into traveling-wave supermodes and standing-wave supermodes based on whether backscattering exists. Coupled-resonator systems can generate traveling-wave supermodes through the evanescent field coupling between optical modes in multiple resonators, enabling applications such as enhanced optomechanical coupling [1–3], stimulated Brillouin laser generation [4,5], Kerr soliton generation [6], phonon lasing [7,8], and the study of parity-time symmetry [9]. In a single microresonator, the degenerate counter-propagating modes couple to each other through backscattering, giving rise to two distinct standing-wave supermodes with a frequency splitting between them [10]. For instance, the presence of a nanoparticle or surface roughness can introduce Rayleigh

scattering, and the ratio of the frequency splitting to the linewidth difference between the two supermodes can be utilized for nanoparticle sizing and counting [11–18]. This detection method requires a distinguishable frequency splitting, typically in the tens to hundreds of MHz range. In this case, the nanoparticle affects all optical modes within the resonator. Furthermore, the introduction of nanometric Bragg gratings to the WGMs through periodic modulation of the periphery allows for the control of the frequency splitting of the mode with a specific azimuthal mode number, which equals half of the modulation period [19,20]. This configuration has been employed to suppress cascaded stimulated Brillouin scattering [21,22], engineer the group velocity dispersion for microcombs [23,24], optical parametric oscillation [25,26], as well as to realize vortex soliton microcombs [5], slow light [27], and generating boundary in the synthetic frequency dimension [28].

For the aforementioned applications utilizing supermode microresonators, the coupling conditions between the microresonators and the coupling waveguides play a crucial role in the detection limit and nonlinear optics processes. For example, in the case of nanoparticle detection, the frequency splitting is required to be greater than the total linewidth of the supermodes, which should be analyzed in an under-coupled regime [11]. In the study of enhanced Brillouin optomechanical coupling using supermode microresonators in Ref. [22], the under-coupled regime was selected for the phonon lasing generation, while the critically-coupled regime was chosen for the Brillouin optomechanical strong coupling process. Surprisingly, the total linewidth of the standing-wave supermode significantly exceeds twice their intrinsic decay rates (κ_0) at critically-coupled conditions. Additionally, it is observed that, even when the external coupling rate ($\kappa_{ex,0}$) is significantly larger than the intrinsic decay rate (coupling parameter $K = \kappa_{ex,0}/\kappa_0 \gg 1$), the over-coupled regime cannot be reached. These behaviors differ from the case of traveling-wave modes, which typically transition through under-coupled ($K < 1$), critically-coupled ($K = 1$), and over-coupled ($K > 1$) regimes as the external coupling rates increase successively.

The total linewidth of the mode at different external coupling rates is related to the coupling ideality (I), which quantitatively describes the efficiency of coupling between a single waveguide mode and a resonator mode. The coupling ideality in traveling-wave mode microresonators such as SiO_2 microspheres [29] and Si_3N_4 microrings [30] has been studied, which can be expressed as

$$I = \frac{\kappa_{ex,0}}{\kappa_{ex,0} + \kappa_p},$$ (1)

where $\kappa_p = \kappa_{HO} + \kappa_{rad}$ is the energy decay rate to the undesired modes, i.e., parasitic losses. κ_{HO} is the external coupling rate between the resonator mode and the higher-order waveguide modes, and κ_{rad} is the waveguide-induced coupling rate to the continuum of radiation modes. Therefore, the coupling ideality determines the relation between the total linewidth ($\kappa_{tot} = \kappa_0 + \kappa_{ex,0} + \kappa_p$) and the on-resonance transmission depth (T) [30,31]:

$$T = \left| 1 - \frac{2}{K^{-1} + I^{-1}} \right|^2$$
$$= 1 - \frac{4I^2(\kappa_0 + \kappa_{tot}(1/I - 1))(\kappa_{tot} - \kappa_0)}{\kappa_{tot}^2}.$$ (2)

Under conditions of phase mismatch between the waveguide mode and resonator mode, the on-resonance transmission cannot reach zero, but can be trimmed by introducing a mode match factor [32]. When $I = 1$ ($\kappa_p = 0$), it refers to ideal coupling, indicating that the total linewidth is twice the intrinsic decay rate at the critically-coupled condition, and the over-coupled regime can be reached. When $I < 1$ ($\kappa_p > 0$), it represents non-ideal coupling, implying that achieving the same on-resonance transmission becomes more challenging due to the requirement of a higher external coupling rate $\kappa_{ex,0}$. Previous studies have demonstrated that a single-mode tapered fiber [29] or waveguide [30] can achieve near-unity ideality for traveling-wave WGMs. In these studies,

parasitic losses were considered primarily attributed to coupling to higher-order modes of the tapered fiber or the waveguide. Nevertheless, the coupling ideality of supermode microresonators, especially in the standing-wave supermode case, warrants further investigation.

In this work, we comprehensively study the coupling ideality of standing-wave supermode microresonators with periodic radius modulation, with the loss channels shown in Fig. 1(a). This structure offers the advantage of precise control of the backscattering coupling rate g in a wide range by adjusting the modulation amplitude, without introducing significant additional decay rate due to the coupling to the reservoir Γ_R. Intriguingly, our findings reveal that the strong backscattering induces additional equivalent parasitic loss. Despite employing a single-mode tapered fiber, the coupling ideality is restricted to 0.5, due to the strong backscattering-induced energy loss into the counter-propagating direction. We have also modified the expression of the coupling ideality in the presence of strong backscattering. Although the equivalent parasitic loss hinders the achievement of over-coupled regimes, it offers a convenient approach to adjust the total linewidth of the modes while preserving the critically-coupled conditions.

2. THEORY

WGM microresonators support degenerate clockwise (CW) and counter-clockwise (CCW) propagating modes, denoted by a_{cw} and a_{ccw}, respectively. In the presence of Rayleigh scatterers, the Heisenberg equations of motion for the optical modes in the rotating frame can be written as [10,11]

$$\begin{bmatrix} \dot{a}_{cw} \\ \dot{a}_{ccw} \end{bmatrix} = \begin{bmatrix} i(\Delta - g) - \frac{\kappa_{tot} + \Gamma_R}{2} & ig + \frac{\Gamma_R}{2} \\ ig + \frac{\Gamma_R}{2} & i(\Delta - g) - \frac{\kappa_{tot} + \Gamma_R}{2} \end{bmatrix} \times \begin{bmatrix} a_{cw} \\ a_{ccw} \end{bmatrix}$$
$$- \sqrt{\kappa_{ex,0}} \begin{bmatrix} a_{cw}^{in} \\ a_{ccw}^{in} \end{bmatrix},$$ (3)

where $\Delta = \omega_L - \omega_c$ is the laser detuning from the cavity resonance with ω_L and ω_c denoting the angular frequencies of the pump laser and the optical mode, respectively. g is the backscattering coupling rate between the CW and CCW modes. Γ_R denotes the additional decay rate due to the coupling to the reservoir [11]. The pump light is coupled into the microresonator through a single-mode tapered fiber, with an amplitude of $a_{cw,ccw}^{in}$. After defining the normal modes inside the microresonator as $a_\pm = (a_{cw} \pm a_{ccw})/\sqrt{2}$, and input modes as $a_\pm^{in} = (a_{cw}^{in} \pm a_{ccw}^{in})/\sqrt{2}$, the steady state solution of the two new normal modes can be expressed as

$$\left(-i(\Delta - 2g) + \frac{\kappa_{tot} + 2\Gamma_R}{2} \right) a_+ + \sqrt{\kappa_{ex,0}} a_+^{in} = 0;$$ (4)

$$\left(-i\Delta + \frac{\kappa_{tot}}{2} \right) a_- + \sqrt{\kappa_{ex,0}} a_-^{in} = 0.$$ (5)

The coupling between the CW and CCW modes leads to two new standing-wave modes, with a frequency difference of $2g/2\pi$ between them, which increases with the backscattering coupling rate, as shown in Fig. 1(b). The inset of Fig. 1(b)
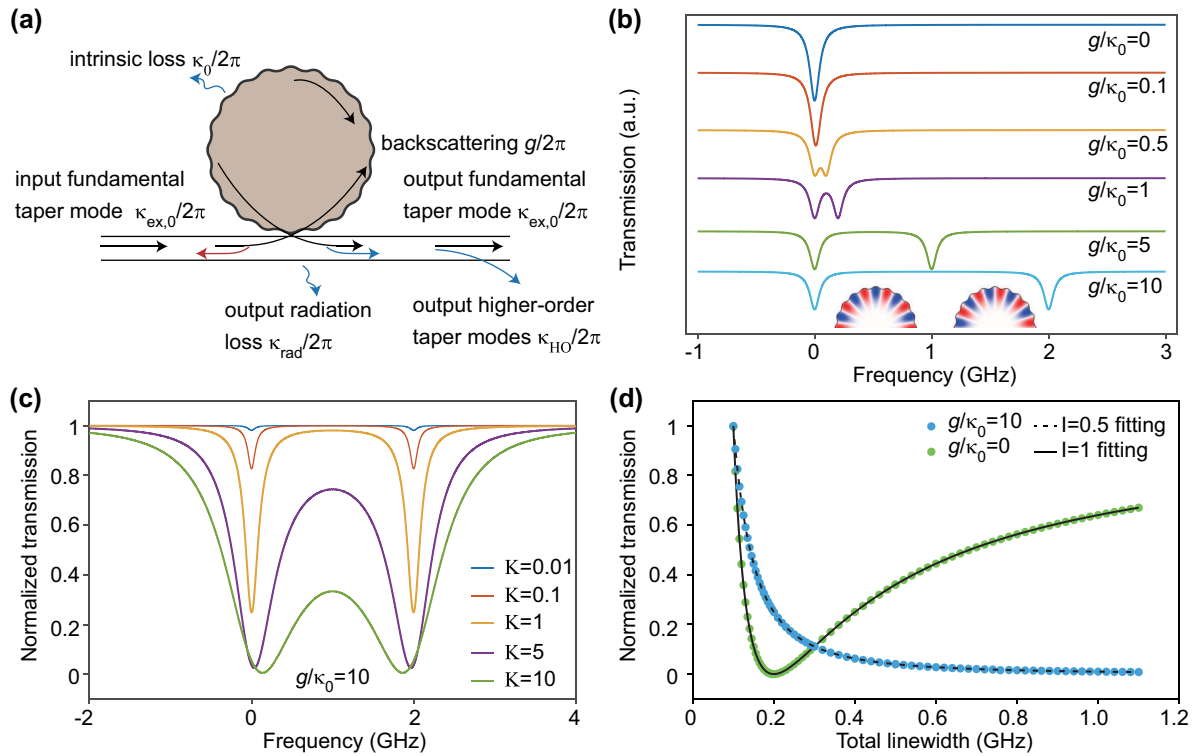
Fig. 1. (a) Schematic of loss channels for standing-wave supermode microresonators with periodic radius modulation. (b) Normalized transmission spectra of the optical modes with the backscattering rate $(g/2\pi)$ increasing from top to bottom, where $\kappa_0/2\pi = 100$ MHz and $\Gamma_R = 0$. Inset: optical field distributions of the two supermodes, with the red and blue colors representing the positive and negative maxima of the electrical field, respectively. (c) Normalized transmission spectra with various external coupling rates $\kappa_{\mathrm{ex},0}/2\pi$. The blue, red, orange, purple, and green curves correspond to $K = \kappa_{\mathrm{ex},0}/\kappa_0 = 0.01, 0.1, 1, 5$, and 10 when $\kappa_0/2\pi = 100$ MHz, $g/\kappa_0 = 10$, respectively. (d) Normalized on-resonance transmission of the optical mode, as a function of the total linewidth. The blue and green dots correspond to the cases with strong backscattering $(g/\kappa_0 = 10)$ and without backscattering $(g/\kappa_0 = 0)$, respectively. The black dashed and solid fitting curves correspond to the ideality of $I = 0.5$ and $I = 1$ cases, respectively.

presents the optical field distributions of the two supermodes. The field maxima of supermode a_+ are located at the minimum radius of the periodic modulation, while those of a_- align with the maximum radius of the modulation. Due to the smaller cavity radius sensed by mode a_+, it resonates at a higher frequency compared to mode a_-. From Eqs. (4) and (5), it is evident that the presence of Γ_R leads to a linewidth increase of the a_+ mode by $2\Gamma_R$, while the a_- mode remains unaffected. Thus, the determination of Γ_R relies on the difference of the intrinsic decay rates between the a_+ and a_- supermodes. However, in the experiment, the observed frequency splitting and linewidth difference between the two supermodes reflect the combined contribution of surface roughness and periodic modulation, making it challenging to separate and characterize each contribution independently. To specifically assess the contribution of Γ_R induced by periodic modulation, we employ finite element method (FEM) simulations to extract the quality factors determined by the radiation loss (Q_{rad}) of both supermodes. The Q_{rad} values for both the a_+ and a_- supermodes exceed 1×10^8. This indicates that the frequency difference between the two supermodes induced by the periodic modulation is less than 2 MHz, which is much smaller than the measured intrinsic linewidths ($\sim$100 MHz) of the supermodes, suggesting a negligible influence of Γ_R induced by periodic modulation.

Therefore, in the numerical simulations in Figs. 1(b)–1(d), we set Γ_R to zero. However, we have retained the parameter Γ_R to ensure the integrity of the equations.

In the absence of the CCW input, the transmission and reflection of the taper-resonator coupled system can be written as

$$T = \left| 1 - \frac{\kappa_{\mathrm{ex},0}\beta}{\beta^2 - (ig + \Gamma_R/2)^2} \right|^2; \qquad (6)$$

$$R = \left| \frac{\kappa_{\mathrm{ex},0}(ig + \Gamma_R/2)}{\beta^2 - (ig + \Gamma_R/2)^2} \right|^2. \qquad (7)$$

Here, β is defined as $\beta = -i\Delta + ig + (\kappa_{\mathrm{tot}} + \Gamma_R)/2$. It can be seen that, when $g = 0$, there is no mode splitting in the transmission and no backscattering signal in the reflection $(R = 0)$. On the contrary, if $g \gg \kappa_{\mathrm{tot}} + \Gamma_R$, the backscattering signal becomes detectable, and significant mode splittings occur in both the transmission and reflection spectra.

Figure 1(c) presents the transmission spectra with strong backscattering $(g/\kappa_0 = 10)$ for different external coupling rates $\kappa_{\mathrm{ex},0}$, with $K = \kappa_{\mathrm{ex},0}/\kappa_0 = 0.01, 0.1, 1, 5$, and 10. For a single-mode taper, κ_{HO} and κ_{rad} are both negligible [29,30], which are therefore set to zero in the simulation. Notably, increasing the $\kappa_{\mathrm{ex},0}$ significantly broadens the linewidth of the two

supermodes while the on-resonance transmission keeps decreasing. When the $\kappa_{ex,0}$ is sufficiently high, e.g., when $K = 10$, slight changes occur in the on-resonance positions of the two supermodes due to the pronounced influence of the wing of the single Lorentzian lineshape on each other. Figure 1(d) depicts the normalized on-resonance transmission as a function of the total linewidth κ_{tot}, with κ_{HO} and κ_{rad} taken as zero. The blue and green dots correspond to the cases with $(g/\kappa_0 = 10)$ and without $(g/\kappa_0 = 0)$ strong backscattering, respectively. The coupling ideality can be obtained through the relation between the on-resonance transmission and the total linewidth, given in Eq. (2). When there is no backscattering $(g/\kappa_0 = 0)$, the ideality equals unity $(I = 1)$, as shown in the black solid fitting curve. However, the presence of strong backscattering $(g/\kappa_0 = 10)$ reduces the ideality to 0.5, as depicted in the black dashed fitting curve, which can be explained as follows.

For the standing-wave supermode microresonator-taper coupled system, the coupling ideality (I) can be redefined as the ratio of the energy coupled into the fundamental taper mode in the CW direction to the total energy coupled into all the output channels induced by the taper:

$$I = \frac{\kappa_{ex,0}}{(\kappa_{ex,0} + \kappa_p)(1 + |a_{ccw}|^2/|a_{cw}|^2)}. \quad (8)$$

Compared with the case without backscattering [29,30], the ideality is modified by a factor of $1/(1 + |a_{ccw}|^2/|a_{cw}|^2)$, in which $|a_{ccw}|^2/|a_{cw}|^2$ is the ratio of the intracavity optical energy in the CCW and CW directions, and can be derived from Eq. (3), as follows:

$$\left|\frac{a_{ccw}}{a_{cw}}\right|^2 = \left|\frac{ig + \frac{\Gamma_R}{2}}{i(\Delta - g) - \frac{\kappa_{tot} + \Gamma_R}{2}}\right|^2. \quad (9)$$

It can be seen from Eqs. (8) and (9) that the ideality is the same for the two supermodes with $\Delta = 2g$ and 0, respectively. In the case of strong backscattering $(g \gg \kappa_{tot} + \Gamma_R)$, $|a_{ccw}|^2/|a_{cw}|^2 \sim 1$, and the ideality can therefore only reach 0.5 even when κ_{HO} and κ_{rad} are both zero. The reason for this additional parasitic loss can also be understood in the following way. The transmission through the tapered fiber is the interference of the partially transmitted input field with the field coupled from the resonator back into the fundamental taper mode. The strong backscattering in the microresonator leads to $1/\sqrt{2}$ of the resonator field (corresponding to 1/2 of the optical energy) backscattered into the counter-propagating direction, which is non-detectable at the transmission spectrum. This results in a distinct on-resonance transmission depth T for each external coupling rate $\kappa_{ex,0}$ compared with the case without backscattering, equivalent to introducing a parasitic loss. The over-coupled regime is difficult to achieve in this scenario. As a comparison, in the case of weak/zero backscattering $(g \ll \kappa_0 + \Gamma_R)$, $|a_{ccw}|^2/|a_{cw}|^2 \sim 0$, and the ideality can reach unity. In this case, the over-coupled regime is attainable. Additionally, the presence of external coupling to higher-order taper modes (κ_{HO}) or radiation modes (κ_{rad}) further decreases the ideality below 0.5 (1) for the strong (weak/zero) backscattering case. Besides, when $g/\kappa_0 < 1$, $|a_{ccw}|^2/|a_{cw}|^2 < 1$, giving rise to a coupling ideality between 0.5 and 1. Conversely,

traveling-wave supermodes in coupled resonators that are generated without relying on backscattering mechanisms do not have this additional equivalent parasitic loss and thus can achieve ideal coupling.

3. EXPERIMENTAL RESULTS

We then use SiO_2 microdisk resonators with periodic radius modulation to experimentally study the coupling ideality of standing-wave supermodes. The radius modulation is in the form of $\alpha \cos(2m\phi)$, with α and ϕ representing the modulation amplitude and azimuthal angle along the cavity boundary, respectively. This modulation selectively splits the targeted mode with an azimuthal mode number m, while leaving all other modes unperturbed [19]. These supermode microresonators are fabricated through electron beam lithography (EBL), inductively coupled plasma (ICP) etching, and XeF_2 etching processes [22]. We fabricated a series of air-cladding SiO_2 supermode microresonators with a thickness of 1 μm, a radius of 20 μm, and modulation amplitude ranging from 10 to 30 nm. In the 1550 nm band, the modulation period of the SiO_2 supermode microresonators is calculated to be $2m = 2 \times 101$. The frequency splitting (Δf) increases with the modulation amplitude, as shown in Fig. 5(a) in Appendix A. The top panel of Fig. 2(a) displays a scanning-electron-microscopy (SEM) image of a 20 μm radius SiO_2 supermode microresonator, with a close-up of the periphery shown in the middle panel, showing an evident sinusoidal radius modulation. A tapered fiber is used to couple light into the microresonator, with an optical microscopy image of the taper-microresonator coupled system shown in the bottom panel of Fig. 2(a). Both transmission and reflection spectra are measured simultaneously by incorporating an optical circulator before the under-tested microresonator.

The identification of the targeted modes is achieved by measuring the frequency splitting of optical modes with different azimuthal mode numbers. Specifically, the targeted modes exhibit substantial mode splitting at the GHz level, distinguishing them from the surface-roughness-induced mode splitting, which is typically at the tens to hundreds of MHz level. Furthermore, the polarization of modes can be identified by examining the magnitude of the frequency splitting of the targeted modes. Transverse magnetic (TM) modes exhibit considerably larger frequency splitting compared to transverse electric (TE) modes due to the larger field distribution of the TM modes at the surface of the microresonator. Figures 2(b) and 2(c) show the normalized transmission (blue) and reflection (orange) spectra for TE and TM modes, respectively, where the targeted modes $(m = 101)$ are identified. To study the coupling ideality of the modes with and without strong backscattering, the two modes marked by the black boxes in Figs. 2(b) and 2(c) are selected, which are labeled as modes a_+, a_-, and mode b, with their fine-scanning spectra shown in Figs. 2(d) and 2(e), respectively. The frequency splitting of the TE-polarized targeted mode is determined to be $\Delta f = 2g/2\pi = 15.7$ GHz, as shown in Fig. 2(d), and the intrinsic decay rates measured at an extremely under-coupled condition are 53.8 MHz and 56 MHz for modes a_+ and a_-, corresponding to intrinsic quality factors of $Q_0 = 3.5 \times 10^6$ and 3.4×10^6,
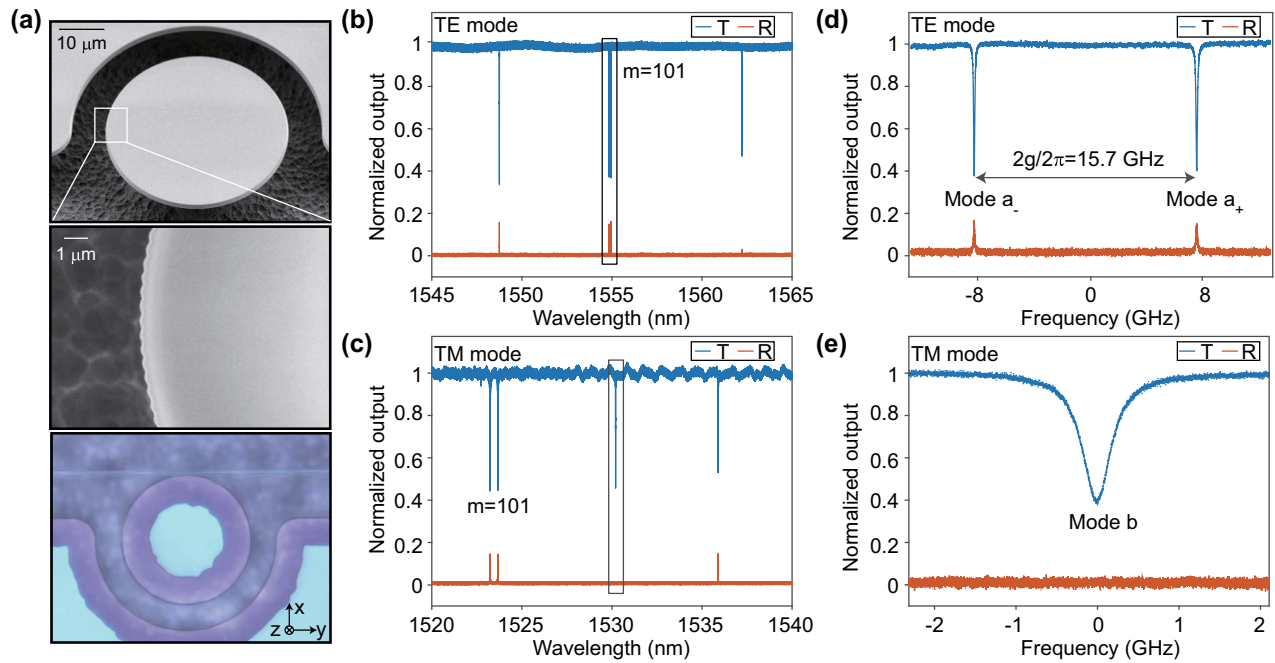
Fig. 2. Characterization of SiO_2 supermode microresonators. (a) Top: scanning electron microscopy (SEM) image of the microresonator. Middle: zoom-in on the periodic radius modulation. Bottom: optical microscopy image of the supermode microresonator coupled with a tapered fiber. (b), (c) Normalized transmission (blue) and reflection (orange) spectra of TE (b) and TM (c) modes of the supermode microresonator. (d), (e) Fine-scanned transmission (blue) and reflection (orange) spectra of modes marked in the black boxes in (b) and (c), respectively.

respectively. The backscattering rate ($g/2\pi$) can be determined by measuring the frequency difference between the two split modes (Δf), which can be quantified as $g/2\pi = \Delta f/2$.

Therefore, the parameter g/κ_0 for supermodes a_+ and a_- is determined to be 135 and 140, respectively. Due to the strong backscattering, a substantial reflection signal is observed. As a
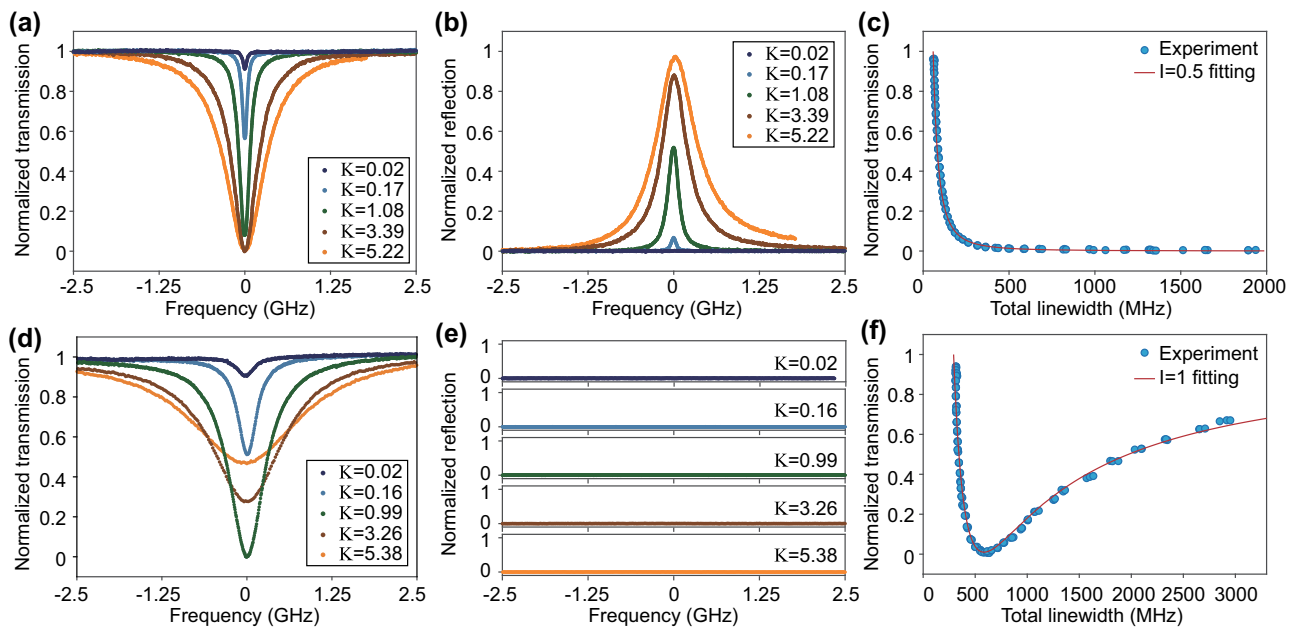

Fig. 3. Measurement of the coupling ideality of SiO_2 supermode microresonators. (a), (b) Evolution of the normalized transmission (a) and reflection (b) spectra of the higher-frequency TE targeted mode (a_+) with $K = 0.02, 0.17, 1.08, 3.39, 5.22$. (c) Normalized on-resonance transmission of the mode a_+ as a function of the total linewidth with a fitting ideality I of 0.5, where $g/\kappa_0 = 135$. (d), (e) Evolution of the normalized transmission spectra (d) and reflection spectra (e) of a non-targeted mode with $K = 0.02, 0.16, 0.99, 3.26, 5.38$, where the backscattering rate is determined to be zero. (f) Normalized on-resonance transmission of the non-targeted mode as a function of the total linewidth with a fitting ideality I of 1, where $g/\kappa_0 = 0$.

comparison, the non-targeted mode (mode b) has no evident frequency splitting ($g = 0$) and thus no reflection signal, as shown in Fig. 2(e). The intrinsic decay rate of mode b is determined to be 292 MHz, corresponding to an intrinsic quality factor of $Q_0 = 0.67 \times 10^6$, giving rise to a zero g/κ_0. It should be noted that mode a is determined to be the targeted fundamental mode, thereby exhibiting a relatively higher quality factor compared with mode b, which is determined to be a higher-order mode. Additionally, the periodic modulation does not introduce any additional decay rate to the supermodes, as the microresonators with and without periodic modulation have similar quality factors, as depicted in Fig. 5(b) in Appendix A.

To mitigate parasitic losses primarily caused by coupling to higher-order taper modes, a single-mode tapered fiber with a diameter smaller than 1.13 µm is employed [33]. The external coupling rate $\kappa_{\mathrm{ex},0}$ is increased by reducing the distance between the microresonator and the tapered fiber along the x- or z-direction, with the coordinate system shown in Fig. 2(a). For the TE-polarized targeted mode a_+, the normalized transmission
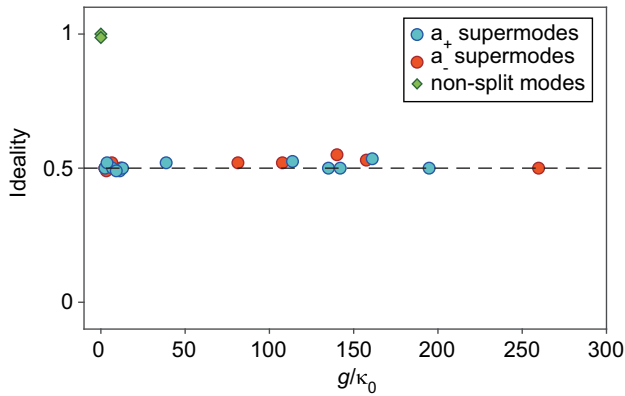
and reflection spectra with five different coupling parameters $K = \kappa_{\mathrm{ex},0}/\kappa_0$ are shown in Figs. 3(a) and 3(b), respectively. It can be seen that, as the external coupling rate increases, the normalized on-resonance transmission decreases from 1 to 0, and remains at 0 even when $K \gg 1$. Although the linewidth of the mode broadens significantly, the mode cannot reach the over-coupled regime. On the other hand, the on-resonance reflection increases from 0 to 0.97 as K increases. Figure 3(c) shows the on-resonance transmission as a function of the total linewidth of this mode, with a fitting curve giving an ideality of $I = 0.5$. The parasitic loss is also equivalent to an increase in the intrinsic decay rate as the external coupling rate increases. For instance, in Fig. 3(a), the intrinsic linewidth of the mode increases from 54.9 MHz at $K = 0.02$ to 276.2 MHz at $K = 5.22$. The normalized transmission and reflection spectra for mode b in the same microresonator with five different coupling parameters K are shown in Figs. 3(d) and 3(e), respectively. It can be seen that, as the external coupling rate increases, the normalized on-resonance transmission first decreases from 1 to 0, and then increases to 0.47 when $K = 5.38$. This mode experiences under-, critically-, and over-coupled regimes successively. On the other hand, as K increases, the reflected signal remains at 0, as shown in Fig. 3(e). The normalized on-resonance transmission as a function of the total linewidth of this mode is shown in Fig. 3(f), with a fitting curve giving an ideality of $I = 1$.

We then measured multiple optical modes in supermode microresonators with modulation amplitudes between 10 and 30 nm, showing varying backscattering coupling rates as shown in Fig. 5(a) in Appendix A. The accuracy for calculating the coupling ideality relies on the resolvability of the two supermodes, specifically requiring the frequency splitting larger than their linewidths. As a result, we study the coupling ideality of the standing-wave supermodes as a function of g/κ_0. To obtain the coupling ideality, we need a range of transmission values as a function of the total linewidth κ_{tot}. For the standing-wave supermodes, as the external coupling rate $\kappa_{\mathrm{ex},0}$ increases, the total linewidth κ_{tot} increases, leading to the merging of the

Fig. 4. Experimental results of the coupling ideality of the supermodes and non-split modes as a function of g/κ_0.
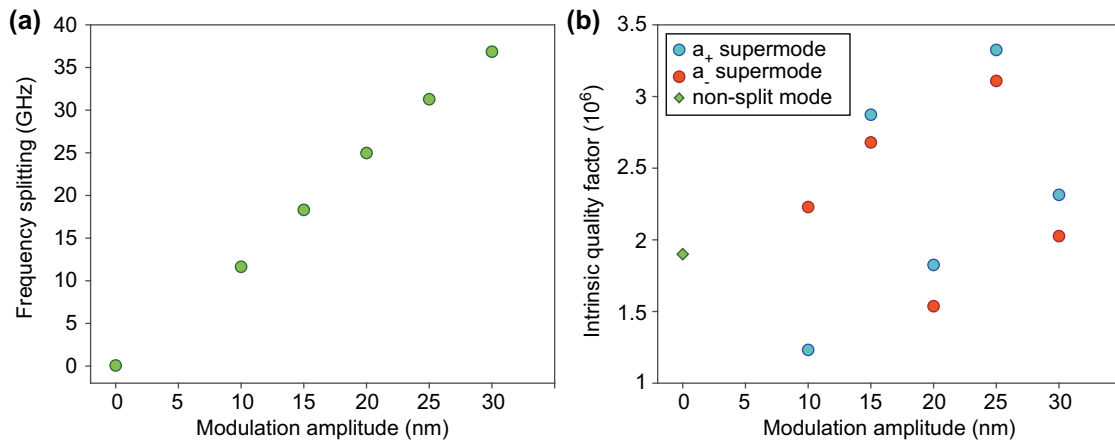

Fig. 5. Characterization of supermode microresonators. (a) Measured frequency splitting and (b) intrinsic quality factors of the optical modes as a function of the modulation amplitude for SiO$_2$ microresonators with a radius of $r_0 = 20$ µm, thickness of 1 µm, and modulation period of $2m = 202$.

two supermodes, which increases the inaccuracy of both the linewidth fitting and the coupling ideality. As a result, to obtain relatively reliable coupling ideality values for the standing-wave supermodes, we only keep the data with g/κ_0 larger than three in our experiments. The statistical results of coupling ideality as a function of g/κ_0 are presented in Fig. 4, with the normalized transmission/reflection spectra and coupling ideality at four different g/κ_0 shown in Fig. 6 in Appendix B. As predicted theoretically, the coupling ideality can reach unity for modes with weak backscattering ($g \ll \kappa_0$), and is limited to around 0.5 for modes with strong backscattering ($g \gg \kappa_0$), even though the diameter of the tapered fiber in the coupling region meets the single-mode criteria.

4. CONCLUSION

We have systematically investigated the coupling ideality of standing-wave supermode microresonators. Both theoretical analysis and experimental results indicate that, for optical modes without observable mode splitting in the case of weak/zero backscattering, the coupling ideality of unity ($I = 1$) can always be achieved by optimizing the coupling conditions. However, in the presence of mode splitting resulting from strong backscattering ($g \gg \kappa_0$), the attainable coupling ideality is limited to $I = 0.5$, thereby impeding the realization of over-coupled regimes. This limitation arises from the fact that the strong backscattering causes half of the optical
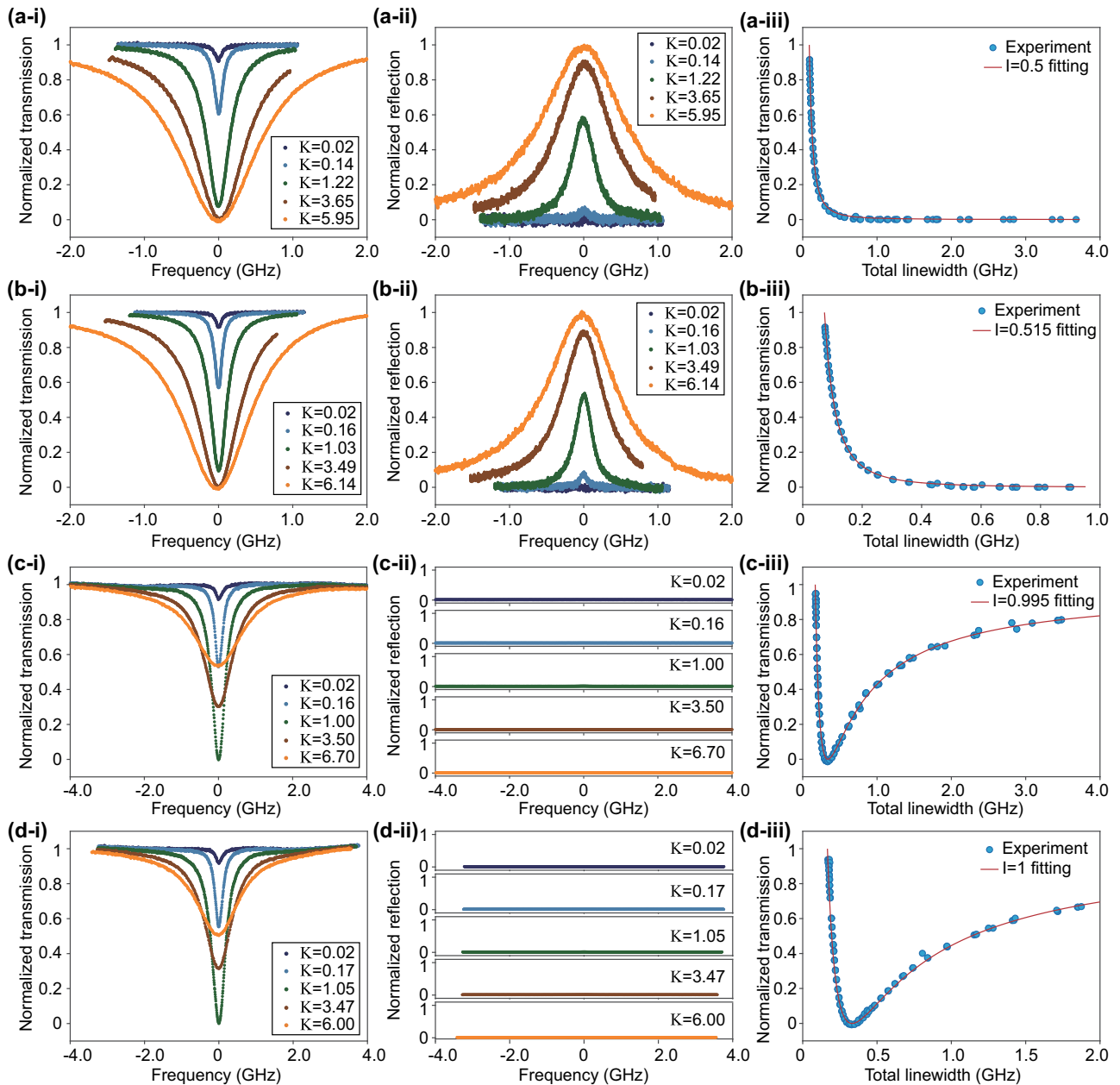

Fig. 6. Measurement of the normalized transmission/reflection spectra and coupling ideality of SiO_2 supermode microresonators. The parameter g/κ_0 for the four modes in (a)–(d) are determined to be 260, 81, 0, and 0, respectively. The left (i), middle (ii), and right (iii) columns show the normalized transmission spectra, normalized reflection spectra, and coupling ideality, respectively.

energy to be backscattered into the counter-propagating direction, introducing an additional equivalent parasitic loss. The coupling ideality of $I = 0.5$ offers a convenient means of adjusting the total linewidth of the standing-wave supermodes while maintaining critically-coupled conditions. This holds promise for controlling the bandwidth of optomechanical sensors, achieving bandwidth-tunable optical filters, and adjusting phase-matching conditions for photon-phonon interactions.

APPENDIX A: CHARACTERIZATION OF SUPERMODE MICRORESONATORS

SiO_2 supermode microresonators with a radius of 20 μm, thickness 1 μm, $2m = 2 \times 101$, and modulation amplitudes in the range of 10–30 nm are experimentally fabricated. Figure 5(a) shows the frequency splitting as a function of the modulation amplitude, from which a monotonic increase can be seen. Owing to the experimentally observed parasitic coupling loss in the system, we initially measured the quality factors of the optical modes with relatively small external coupling rates, maintaining the on-resonance transmission depth at around 0.9. Figure 5(b) shows the intrinsic quality factors of several microresonators with different modulation amplitudes on the same chip. It can be seen that all the intrinsic quality factors are at the level of 1×10^6, for microresonators with and without the periodic modulation. This suggests that the introduction of periodic modulation did not decrease the intrinsic quality factors of the supermode microresonators. The measured intrinsic quality factors are considered to be limited by the surface-roughness-induced scattering loss.

APPENDIX B: CHARACTERIZATION OF COUPLING IDEALITY

For the optical modes we studied in Fig. 4, we also include their normalized transmission and reflection spectra, as well as their coupling ideality, four of which are plotted in Fig. 6, with g/κ_0 determined to be 260, 81, 0, and 0.

Disclosures. The authors declare no conflicts of interest.

Data Availability. Data underlying the results presented in this paper are not publicly available at this time but may be obtained from the authors upon reasonable request.

REFERENCES

1. J. Rosenberg, Q. Lin, and O. Painter, "Static and dynamic wavelength routing via the gradient optical force," Nat. Photonics **3**, 478–483 (2009).
2. G. S. Wiederhecker, L. Chen, A. Gondarenko, *et al.*, "Controlling photonic structures using optical forces," Nature **462**, 633–636 (2009).
3. Y. Lei, Z.-G. Hu, M. Wang, *et al.*, "Fully reconfigurable optomechanical add-drop filters," Appl. Phy. Lett. **121**, 181110 (2022).
4. Y. A. Espinel, F. G. Santos, G. O. Luiz, *et al.*, "Brillouin optomechanics in coupled silicon microcavities," Sci. Rep. **7**, 43423 (2017).
5. Y. Liu, C. Lao, M. Wang, *et al.*, "Integrated vortex soliton microcombs," Nat. Photonics (2024).
6. A. Tikan, A. Tusnin, J. Riemensberger, *et al.*, "Protected generation of dissipative Kerr solitons in supermodes of coupled optical microresonators," Sci. Adv. **8**, eabm6982 (2022).
7. I. S. Grudinin, H. Lee, O. Painter, *et al.*, "Phonon laser action in a tunable two-level system," Phys. Rev. Lett. **104**, 083901 (2010).
8. G. Wang, M. Zhao, Y. Qin, *et al.*, "Demonstration of an ultra-low-threshold phonon laser with coupled microtoroid resonators in vacuum," Photon. Res. **5**, 73–76 (2017).
9. B. Peng, Ş. K. Özdemir, F. Lei, *et al.*, "Parity–time-symmetric whispering-gallery microcavities," Nat. Phys. **10**, 394–398 (2014).
10. A. Mazzei, S. Götzinger, L. D. S. Menezes, *et al.*, "Controlled coupling of counterpropagating whispering-gallery modes by a single Rayleigh scatterer: a classical problem in a quantum optical light," Phys. Rev. Lett. **99**, 173603 (2007).
11. J. Zhu, S. K. Ozdemir, Y.-F. Xiao, *et al.*, "On-chip single nanoparticle detection and sizing by mode splitting in an ultrahigh-Q microresonator," Nat. Photonics **4**, 46–49 (2010).
12. L. He, Ş. K. Özdemir, J. Zhu, *et al.*, "Detecting single viruses and nanoparticles using whispering gallery microlasers," Nat. Nanotechnol. **6**, 428–432 (2011).
13. L. He, Ş. K. Özdemir, J. Zhu, *et al.*, "Statistics of multiple-scatterer-induced frequency splitting in whispering gallery microresonators and microlasers," New J. Phys. **15**, 073030 (2013).
14. B.-B. Li, W. R. Clements, X.-C. Yu, *et al.*, "Single nanoparticle detection using split-mode microcavity Raman lasers," Proc. Natl. Acad. Sci. USA **111**, 14657–14662 (2014).
15. Y. Zhi, X.-C. Yu, Q. Gong, *et al.*, "Single nanoparticle detection using optical microcavities," Adv. Mater. **29**, 1604920 (2017).
16. J. Zhu, Ş. K. Özdemir, L. He, *et al.*, "Controlled manipulation of mode splitting in an optical microcavity by two Rayleigh scatterers," Opt. Express **18**, 23535–23543 (2010).
17. P.-J. Zhang, Q.-X. Ji, Q.-T. Cao, *et al.*, "Single-mode characteristic of a supermode microcavity Raman laser," Proc. Natl. Acad. Sci. USA **118**, e2101605118 (2021).
18. W. R. Clements, B.-B. Li, B.-Q. Shen, *et al.*, "Raman-lasing dynamics in split-mode microresonators," Phys. Rev. A **91**, 013804 (2015).
19. X. Lu, S. Rogers, W. C. Jiang, *et al.*, "Selective engineering of cavity resonance for frequency matching in optical parametric processes," Appl. Phys. Lett. **105**, 151104 (2014).
20. X. Lu, A. Rao, G. Moille, *et al.*, "Universal frequency engineering tool for microcavity nonlinear optics: multiple selective mode splitting of whispering-gallery resonances," Photon. Res. **8**, 1676–1686 (2020).
21. M. Puckett, D. Bose, K. Nelson, *et al.*, "Higher order cascaded SBS suppression using gratings in a photonic integrated ring resonator laser," in *CLEO: Science and Innovations* (Optica, 2019), paper SM4O-1.
22. M. Wang, Z.-G. Hu, C. Lao, *et al.*, "Taming Brillouin optomechanics using supermode microresonators," Phys. Rev. X **14**, 011056 (2024).
23. S.-P. Yu, D. C. Cole, H. Jung, *et al.*, "Spontaneous pulse formation in edgeless photonic crystal resonators," Nat. Photonics **15**, 461–467 (2021).
24. S.-P. Yu, E. Lucas, J. Zang, *et al.*, "A continuum of bright and dark-pulse states in a photonic-crystal resonator," Nat. Commun. **13**, 3134 (2022).
25. X. Lu, A. Chanana, F. Zhou, *et al.*, "Kerr optical parametric oscillation in a photonic crystal microring for accessing the infrared," Opt. Lett. **47**, 3331–3334 (2022).

26. X. Lu, Y. Sun, A. Chanana, *et al.*, "Multi-mode microcavity frequency engineering through a shifted grating in a photonic crystal ring," Photon. Res. **11**, A72–A79 (2023).

27. X. Lu, A. McClung, and K. Srinivasan, "High-*Q* slow light and its localization in a photonic crystal microring," Nat. Photonics **16**, 66–71 (2022).

28. K. Zhang, Y. Chen, W. Sun, *et al.*, "Spectral engineering of optical microresonators in anisotropic lithium niobate crystal," Adv. Mater. **36**, 2308840 (2024).

29. S. Spillane, T. Kippenberg, O. Painter, *et al.*, "Ideality in a fiber-taper-coupled microresonator system for application to cavity quantum electrodynamics," Phys. Rev. Lett. **91**, 043902 (2003).

30. M. H. Pfeiffer, J. Liu, M. Geiselmann, *et al.*, "Coupling ideality of integrated planar high-*Q* microresonators," Phys. Rev. Appl. **7**, 024026 (2017).

31. Z. Ye, H. Jia, Z. Huang, *et al.*, "Foundry manufacturing of tight-confinement, dispersion-engineered, ultralow-loss silicon nitride photonic integrated circuits," Photon. Res. **11**, 558–568 (2023).

32. M. L. Gorodetsky and V. S. Ilchenko, "Optical microsphere resonators: optimal coupling to high-*Q* whispering-gallery modes," J. Opt. Soc. Am. B **16**, 147–154 (1999).

33. J. C. Knight, G. Cheung, F. Jacques, *et al.*, "Phase-matched excitation of whispering-gallery-mode resonances by a fiber taper," Opt. Lett. **22**, 1129–1131 (1997).